Open Ceramics 12 (2022) 100306

Contents lists available at ScienceDirect

Open Ceramics

journal homepage: www.sciencedirect.com/journal/open-ceramics

Macroporous silicon-wollastonite scaffold with Sr/Se/Zn/Mg-substituted hydroxyapatite/chitosan hydrogel

Antonia Ressler [a,*], Nikhil Kamboj [b,c], Maja Ledinski [d], Anamarija Rogina [a], Inga Urlić [d], Irina Hussainova [b], Hrvoje Ivanković [a], Marica Ivanković [a]

[a] Faculty of Chemical Engineering and Technology, University of Zagreb, HR-10000, Zagreb, Marulićev trg 19, Croatia
[b] Tallinn University of Technology, Department of Mechanical and Industrial Engineering, Ehitajate 5, 19086, Tallinn, Estonia
[c] Turku Clinical Biomaterials Centre, Department of Biomaterials Science, Faculty of Medicine, Institute of Dentistry, University of Turku, FI-20014, Turku, Finland
[d] Faculty of Science, University of Zagreb, Horvatovac 102a, Zagreb, 10 000, Croatia

ARTICLE INFO

Keywords:
Bone regeneration
Chitosan
Hydroxyapatite
Ion substitution
Scaffold
Selective laser melting
Wollastonite

ABSTRACT

The scaffolds, which morphologically and physiologically mimic natural features of the bone, are of a high demand for regenerative medicine. To address this challenge, bioactive porous silicon/wollastonite (SC) scaffold has been developed for potential bone tissue engineering applications. Additive manufacturing through the selective laser melting approach has been exploited to fabricate computer-aided designed scaffolds with a pore size of 400 μm. To increase the biocompatibility and osteogenic properties of SC scaffolds, the hydrogel based on a mixture of four mono-substituted hydroxyapatites (sHAp) and biopolymer chitosan (CHT) has been incorporated into SC by impregnation and freeze-gelation method. The pore size of 400 μm of SC has provided enough space for the impregnation of polymer solution and composite (CHT/sHAp) suspension to form highly porous hydrogel within pores. By the combination of SC and CHT/sHAp, both cell attachment and homogeneous proliferation on SC scaffold as well as mechanical properties of CHT/sHAp hydrogel have been improved.

1. Introduction

The natural bone tissue is composed of a mineralogical phase, calcium-deficient carbonated hydroxyapatite (HAp), which represents 65–70% of the matrix and an organic phase (collagen, glycoproteins, proteoglycans, sialoproteins, etc.), which comprises the remaining 25–30% of the total bone matrix [1]. The natural HAp is substituted with various ions (e.g. Na^{+}, Mg^{2+}, Sr^{2+}, Mg^{2+}, Zn^{2+}, K^{+}, CO_3^{2-}), which are highly important for the physiochemical and biological properties of a hard tissue [2]. The biomimetic approach is a new pathway in bone tissue engineering requiring bio-mimicry of the natural bone tissue in chemical composition, physical structure and mechanical properties [3].

As biological apatites are characterized by various ionic substitutions that are crucial for bone metabolism, a large number of studies are focused on the synthesis and characterization of biomimetic ionic substituted HAp to be used as a bioactive phase in biomaterials for bone regeneration [4]. The flexible hexagonal structure of HAp can incorporate a great variety of cationic (Sr^{2+}, Na^{+}, K^{+}, Mg^{2+}, Zn^{2+}, Ag^{+}, etc.) and anionic (CO_3^{2-}, SiO_4^{4-}, SeO_3^{2-}, SeO_4^{2-}, F^{-}, Cl^{-}, Br^{-}, etc.) substitutions [5]. The introduction of trace elements within HAp lattice and bone grafts can lead to antimicrobial, osteogenic, and anticancer properties obtained by selective substitutions and mimicking the elemental content of biological apatites [6]. As a lot of efforts are put into mimicking the inorganic phase of the bone tissue, the same effort is directed towards mimicking the organic phase, which later combination leads to composite material with a similar complex structure as natural bone tissue. Naturally derived polymers (e.g. collagen, gelatin, chitosan, glycosaminoglycans, silk fibrin) have been widely used in a variety of tissue engineering applications as they can mimic natural extracellular matrix. As natural polymers are building components of biological tissues, they demonstrate excellent biocompatibility *in vivo* and present a range of ligands and peptides that facilitate cell adhesion and osteogenic differentiation [3]. One of the most widely studied biopolymers is chitosan (CHT), a natural amino polysaccharide with a unique structure and multidimensional properties suitable for a wide range of applications in biomedicine [7]. It is composed of randomly distributed β-(1–4)-linked D-glucosamine (glucosamine) and *N*-acetyl-D-glucosamine (*N*-acetylglucosamine) structure units, structurally similar to glycosaminoglycan, a

* Corresponding author. Faculty of Chemical Engineering and Technology, University of Zagreb, HR-10000, Zagreb, Marulićev trg 19, p.p.177, Croatia.
E-mail addresses: aressler@fkit.hr (A. Ressler), nikhil.kamboj@taltech.ee, nikhil.kamboj@utu.fi (N. Kamboj), maja.ledinski@biol.pmf.hr (M. Ledinski), arogina@fkit.hr (A. Rogina), inga.urlic@biol.pmf.hr (I. Urlić), irina.hussainova@taltech.ee (I. Hussainova), hivan@fkit.hr (H. Ivanković), mivank@fkit.hr (M. Ivanković).

https://doi.org/10.1016/j.oceram.2022.100306
Received 7 June 2022; Received in revised form 1 September 2022; Accepted 16 September 2022
Available online 20 September 2022

key component of the bone matrix and cell surface that modulate the bioavailability and activity of various osteoclastic and osteogenic factors [4,8–10]. Biopolymer CHT can be considered as a linear polyelectrolyte with a high charge density which can interact with negatively charged species (e.g. proteins) [11]. Chitosan and hydroxyapatite-based composites (CHT/HAp) have been widely studied as potential scaffolds for bone tissue engineering (BTE) applications. However, the CHT/HAp scaffolds can be used for the bone regeneration process at bone defects that are placed in the part of the human bone which is not subject to mechanical stresses and loads [3,12]. The challenge of BTE is to develop a scaffold with appropriate porosity, pore size distribution and mechanical strength to allow the cell migration, adhesion, growth, proliferation and differentiation into the osteoblast phenotype [3,13]. The highly porous scaffold based on CHT and HAps substituted with Sr^{2+}, Mg^{2+}, Zn^{2+} and SeO_3^{2-} ions (sHAp) has been studied in our previous research [14]. It has been determined that CHT/sHAp composite scaffold acts as three-dimensional (3D) support for human mesenchymal stem cells proliferation and differentiation into osteoblasts cells. Expression of characteristic bone genes, alkaline phosphatase, bone sialoprotein, collagen type I, dentin matrix protein I and phosphate deposits, along with newly formed bone tissue, indicated that extracellular matrix mineralization took place during 21 days of cell culture [14].

The aim of the present research is to produce a 3D scaffold with suitable microstructure, bioactive components, biocompatibility and mechanical properties for bone tissue defects where mechanical support for surrounding tissue is needed. Two previously obtained materials were combined to meet desired properties of the final scaffold [14,15]. The 3D scaffold based on silicon and pseudowollastonite (high--temperature polymorph of wollastonite) has been produced by the selective laser melting (SLM) method and used as a bioactive construct demonstrating the appropriate characteristics for a potential application in hard tissue engineering [15]. To further increase the osteogenic ability of silicon/pseudowollastonite scaffolds (SC) and increase the mechanical performance of CHT/sHAp composite, CHT/sHAp was incorporated in SC scaffold by impregnation and freeze-gelation method. A mixture of mono-substituted HAps (with Sr^{2+}, Zn^{2+}, Mg^{2+} and SeO_3^{2-} ions) was used to mimic natural HAp. To the best of our knowledge, this is the first time that a highly porous scaffold based on CHT/sHAp is combined with scaffolds obtained by the SLM method.

2. Materials and methods

2.1. Silicon-wollastonite scaffold fabrication

The SC scaffold was fabricated according to our previous study [15]. In brief, the 3D scaffold of 6 mm in height and 5 mm in diameter was fabricated according to a computer aided design (CAD) with a pore diameter of 400 μm. The mixture of silicon (30 wt%) and wollastonite (70 wt%) was used as fabricating material. Scaffolds were fabricated by the 3D printer (ReaLizer GmbH SLM-50) with optimized process parameters with a layer thickness of 25 μm, hatch distance of 60 μm, and point distance of 10 μm at a scanning speed of 80 mm/s. The process was performed in argon atmosphere (99.999 vol%) to avoid the formation of undesirable crystalline phases. After 3D fabrication, loose powder adhered to the scaffolds was removed by a sonication process for 15 min in ethanol.

2.2. Chitosan/substituted-hydroxyapatite suspension

The cuttlefish bones (*Sepia officinalis L.*) from the Adriatic Sea were heat treated at 800 °C for 3 h in order to obtain calcium oxide (CaO) from calcium carbonate ($CaCO_3$) and remove the organic matrix. The CaO obtained from cuttlefish bones has been used as a source of Ca^{2+} ions for HAp precipitation.

The mono-substituted HAp powders (with 5 mol% of Sr^{2+}, SeO_3^{2-}, Zn^{2+} and Mg^{2+} ions) were synthesized by the wet precipitation method according to our previous studies with minor changes [14]. In brief, the HAp was prepared by dissolving the CaO and strontium nitrate ($Sr(NO_3)_2$, Sigma-Aldrich), sodium selenite pentahydrate ($Na_2SeO_3 \cdot 5H_2O$, Sigma Aldrich), zinc nitrate hexahydrate ($Zn(NO_3)_2 \cdot 6H_2O$, Honeywell) or magnesium chloride hexahydrate ($MgCl_2 \cdot 6H_2O$, KEMIG) in demineralized water. Urea phosphate (UPH, $CO(NH_2)_2$–H_3PO_4, Sigma-Aldrich) was added into the solution to gain (Ca + Sr)/P and Ca/(P + Se) molar ratio 1.67, required for stoichiometric HAp. Stirring was continued for 5 days at 50 °C followed by overnight aging at room temperature (T = 23.5 °C ± 0.5). Ammonium dihydrogen phosphate ($NH_4H_2PO_4$; Lachner) was added into the solution to gain (Ca + Zn)/P and (Ca + Zn)/P molar ratio 1.67. Stirring was continued for 3 days at 60 °C followed by overnight aging at room temperature. The final pH values of all prepared suspensions were higher than 8, favorable for HAp formation [16]. The corresponding concentrations of the reactants in the starting reaction solutions are listed in Table 1. Supernatant and HAp particles were separated by filtering without washing and dried at room temperature (T = 23.5 °C ± 0.5). The powdered samples were prepared by hand grinding using a mortar and pestle. The as-prepared mono--substituted HAp powders were used for obtaining CHT/sHAp composite scaffolds. The mass fraction of each mono-substituted HAp in the HAp mixture, used for obtaining the composite, was the same (25 wt%). The HAp mixture of mono-substituted HAps was homogenized by hand grinding using a mortar and pestle in ethanol for 15 min.

The appropriate amount of chitosan was added to 0.40 wt% acetic acid solution to obtain 1.2 wt% chitosan solution at ambient temperature. The appropriate amount of HAp mixture was added to obtain HAp/chitosan weight ratio of 30/70. Mixture of HAp powders and chitosan solution were homogenized for 10 min by stirring at 1700 rpm and 5 min in the ultrasonic bath.

2.3. Composite scaffold

Porous composite scaffolds were obtained by the freeze-gelation method as reported previously with slight modification [17]. The 3D fabricated SC scaffolds were impregnated with CHT solution and CHT/sHAp suspension under vacuum (p = 0.12 bar) for 20 min by impregnation pump (CitoVac, Struers). The used volume of CHT solution and CHT/sHAp suspension for SC scaffolds impregnation was selected to fully cover scaffolds in the vacuum chamber. After impregnation, scaffolds were frozen (−30 °C) and subsequently immersed into a gelation medium of 1 M NaOH/ethanol at −30 °C for 24 h to induce the gelation of chitosan. The samples were rinsed in ethanol (96 wt%) at −30 °C for 24 h, washed with distilled water, frozen, and freeze-dried (Kambič, LIO-5 PLT). The non-impregnated SC scaffold was used as a control. The composite scaffold preparation is illustrated in Fig. 1. Obtained composite scaffolds based on silicon (Si), pseudowollastonite (PWoll), CHT and sHAp are referred as described in Table 2.

2.4. Scaffolds characterization

The mixture of mono-substituted HAp powders (sHAp) was characterized by X-ray diffraction (XRD) analysis using Shimadzu XRD-6000 diffractometer with Cu Kα (1.5406 Å) radiation operated at 40 kV and

Table 1
Quantities of reactants for the synthesis of substituted HAp powders.

	CaO (mM)	UPH/$NH_4H_2PO_4$ (mM)	Substituents precursors (mM)
5 mol% Sr^{2+}	181.00	114.09	9.53
5 mol% Zn^{2+}	181.00	114.09	9.53
5 mol% Mg^{2+}	181.00	114.09	9.53
5 mol% SeO_3^{2-}	199.00	113.05	6.11

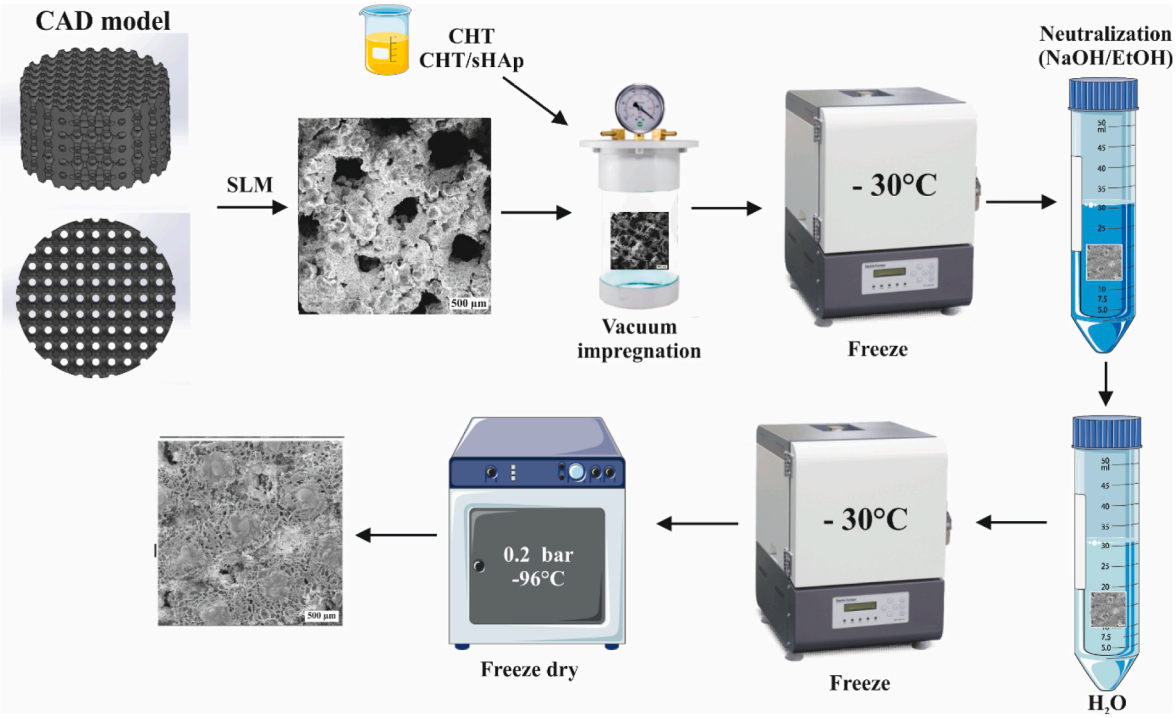

Fig. 1. Schematic illustration SC_CHT/sHAp scaffolds preparation. The first step involves 3D printing of SC scaffold by SLM method, followed by impregnation of CHT/sHAp suspension and freeze gelation. The final step includes washing, freezing and freeze drying.

Table 2
Composite scaffolds based on silicon-pseudowollastonite, chitosan and multi-substituted HAp.

Phase composition	Substitution level (mol%)	Scaffold
Si, PWoll	–	SC
Si, PWoll, CHT	–	SC_CHT
Si, PWoll, CHT, sHAp	5 mol% Sr^{2+}, SeO_3^{2-}, Mg^{2+}, Zn^{2+}	SC_CHT/sHAp

30 mA. The diffraction patterns were collected in the 2θ range 20–60°, with a step size of 0.02° and exposure of 2 s. Whole-powder-pattern decomposition refinement studies were performed as previously described in our studies [18] using the software DIFFRAC.SUITE TOPAS V.5.0. with the fundamental parameters approach. Identification of the phases was performed by comparing the experimental XRD patterns to standards compiled by the International Centre for Diffraction Data. For HAp the ICDD card 09–432 was used. The structural parameters of HAp, reported by Veselinović et al. [19] have been used as the initial values in the refinements.

The morphology of composite scaffolds was imaged by the scanning electron microscope Zeiss EVO MA 15 (SEM) at electron beam energy of 10 keV. Previously to imaging, samples were sputter coated with gold and palladium for 120 s. The SEM equipped with EDS (SEM Zeiss EVO Ma 15) with a voltage of up 20 kV was used to determine the elemental composition of prepared scaffolds.

The Fourier transform infrared spectra (FTIR) of composite scaffolds were recorded by attenuated total reflectance (ATR) spectrometer for solids with a diamond crystal (Bruker Vertex 70) at 20 °C over the spectral range of 4000–400 cm^{-1}, with 32 scans and 4 cm^{-1} of resolution. The FTIR spectra of CHT and HAp were used as controls.

Thermogravimetric (TGA) and differential scanning calorimetry (DCS) analyses were performed on Netzch STA 409 instrument. Measurements were performed with a constant synthetic air flow of 30 cm^3 min^{-1} from 20 °C to 1000 °C at a heating rate of 10 °C min^{-1}.

2.5. Compression tests

The cylindrical porous samples of 6 mm in diameter and 5 mm in height were tested under compression using the servo-hydraulic model 8500 universal testing machine (Instron Itd.) at applied strain rate of 0.5 mm min^{-1}. The compressive load and displacement were recorded at each 0.1 s intervals during testing. Maximum compressive strength was determined using software associated with the testing machine. All the compressive strength measurements on the scaffolds were performed at room temperature (T = 22.5 °C ± 0.5) and the measurements were performed in triplicates.

2.6. Biological evaluation

Obtained scaffolds were sterilised in 96% ethanol for 24 h. After sterilisation, scaffolds were washed 4 times with phosphate buffer saline (PBS, Gibco, Thermo Fisher Scientific) and transported into polystyrene 24-well plate with a hydrophobic surface (Corning, Sigma Aldrich).

Cell suspension of the human embryonic kidney 293 (HEK 293) cells was applied on each scaffold in a concentration of $5{\cdot}10^6$ cells/20 µL in Dulbecco's Modified Eagle Medium (high glucose) with 10% FBS and 1% penicillin/streptomycin (Capricon). Scaffolds with seeded cells were incubated for 30 min in the cell culture incubator to allow cell attachment and migration inside the scaffold. Following the incubation period, the medium was added to a final volume of 1 mL per well. The cells were kept in a humidified atmosphere with 5% CO_2 at 37 °C and the culture medium was changed every three days.

Qualitative cell viability and distribution were evaluated by live/dead assay using Live/Dead® Viability/Cytotoxicity Kit (Invitrogen) after 1 and 7 days of cell culture. Cultured samples were washed two times with sterile PBS and incubated with 2 µmol/L calcein acetoxymethyl (calcein-AM) and 4 µmol/L ethidium homodimer (EthD1) in a humidified atmosphere with 5% CO_2 at 37 °C for 30 min. Live cells (stained in green) and dead cells (stained in red) were analysed by fluorescence microscope Axiovert 200 M (Zeiss, Göttingen) with AxioVision software 4.5.

2.7. Statistical analysis

The values for mechanical analysis were presented as the mean ± standard deviation and analysed with Student's *t*-test, in which differences were considered statically significant when $p < 0.05$ and $p < 0.01$.

3. Results and discussion

3.1. Trace elements in HAp powder

The XRD pattern of the mixture of mono-substituted HAps (Fig. 2a) shows characteristic peaks of the crystalline HAp phase (ICDD 09–0432). No additional peaks characteristic for strontium, selenium, magnesium and zinc compounds are observed. EDX analysis has been used to confirm the atomic composition of the HAp mixture. EDX spectra (Fig. 2b) confirmed the presence of Sr^{2+}, Mg^{2+}, Zn^{2+} and SeO_3^{2-} ions. In addition, Na^+ ions were detected as a result of using cuttlefish bone as a source of Ca^{2+} ions. In our previous research [18], the chemical composition of non-substituted HAp obtained from cuttlefish bone (CaO) was determined by inductively coupled plasma mass spectrometry (ICP-MS) and the presence of Sr^{2+} (0.49 mol%), Mg^{2+} (0.60 mol%) and Na^+ (0.74 mol%) substitutions were confirmed. Detected carbon might be related to the presence of CO_3^{2-} substitution in HAp lattice [18]. As the HAp powders were synthesized from CaO, CO_3^{2-} substitution in HAp lattice is a result of the high reactivity of Ca^{2+} precursor and the presence of CO_2 in the process of synthesis at atmospheric conditions. The trace elements have been found to play a key role in bone regeneration. Zn^{2+} and Sr^{2+} ions have a dual mode of action where they stimulate the osteoblastic bone-building process and inhibit the osteoclastic resorption process [6]. Mg^{2+} ions are crucial in the early stage of bone formation, while SeO_3^{2-} ions have shown anti-tumor, anti-oxidant and anti-bacterial effects which are highly important for materials with potential applications in bone tissue engineering [20–22]. By selecting target ions and optimization of substitution levels, the produced materials can have unique properties for specific applications; for example, osteogenic biomaterial with antibacterial and selective anticancer properties can be obtained.

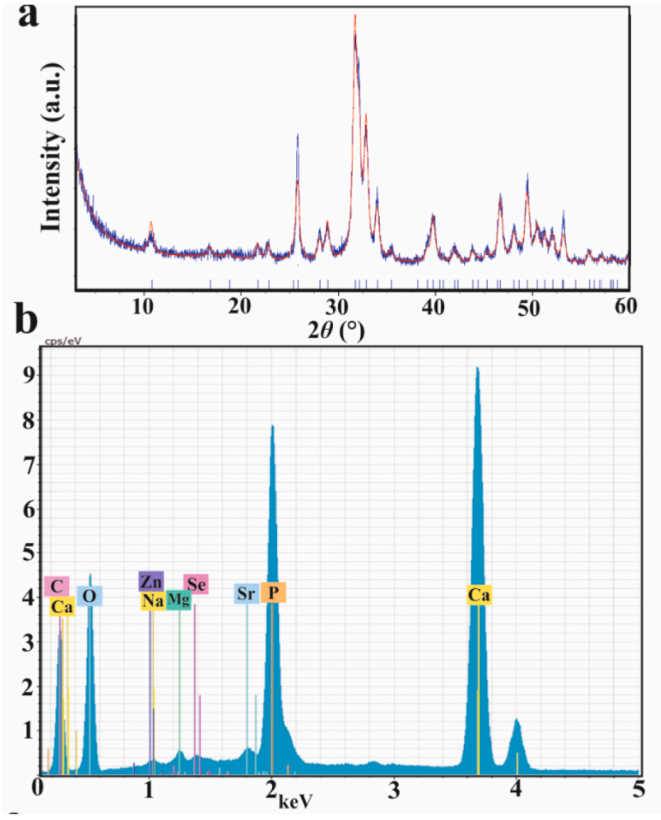

Fig. 2. (a) Whole-powder-pattern decomposition refinement study of the powder X-ray diffraction pattern. The blue line is experimental data and the red line calculated intensities. (b) EDX of the mixture of four mono-substituted HAps (sHAp). (For interpretation of the references to colour in this figure legend, the reader is referred to the Web version of this article.)

3.2. Composite scaffolds microstructure

The microstructure of prepared composite scaffolds (SC, SC_CHT and SC_CHT/sHAp) has been examined by SEM imaging (Fig. 3). As shown in Fig. 3a, the SC scaffold with a pore size of ~400 μm (depicted in red) replicated the scaffolds microstructure specified with CAD 3D design as reported in our work [15]. The microstructures of composite scaffolds reveal highly porous structures with interconnected pores of the chitosan in SC_CHT (Fig. 3b), with homogeneously dispersed HAp particles in the polymer matrix observed in SC_CHT/sHAp scaffold (Fig. 3c). As previously determined in our study [14], the freeze-gelation of CHT/sHAp solution leads to the formation of the pores in the range from ~35 to ~350 μm. The pore size of 400 μm of SC has provided enough space for the impregnation of polymer solution and the formation of highly porous hydrogel within SC pores. The macroporosity (>100–400 μm) and pore interconnectivity pathways promote osteogenesis by enhancing cell migration, vascularization and diffusion of nutrients, oxygen and metabolic waste, while microporosity (<20 μm) is important for cell seeding, capillaries growth and cell-cell interactions [3].

3.3. FTIR analysis

FTIR spectra (Fig. 4) of the prepared scaffolds and controls (CHT and HAp) are shown in the range 400–1200 cm^{-1}, where all bands significant for the developed materials were detected. HAp powder shows characteristic phosphate (PO_4^{3-}) bands at 1020 and 1072 cm^{-1} (ν_3, attributed to the asymmetric stretching vibration of P–O), 557 and 602 cm^{-1} (ν_4, attributed to asymmetric bending vibrations of O–P–O) and 956 cm^{-1} (ν_1, associated to the symmetric stretching vibration of P–O) [23]. Additionally, the absorption bands at 525, 918 and 1113 cm^{-1} are attributed to the characteristic absorption of a HPO_4^{2-} group that can be assigned to the amorphous calcium phosphate (ACP) phase [24]. In our previous study [18], when CaO obtained from cuttlefish bone has been used for HAp precipitation, 11.38 wt% of ACP phase has been detected along with HAp. However, detected HPO_4^{2-} group cannot only be associated with ACP phase as HPO_4^{2-} substitutions are possible within HAp lattice, as well. Absorption band at 875 (ν_2, out of plane bending) is ascribed to the carbonate (CO_3^{2-}) ions indicating that tetrahedral PO_4^{3-} sites in the HAp lattice are replaced partially by CO_3^{2-} (B-type of substitution) typical for biological apatite [25]. FTIR spectra of CHT show typical bands of chitosan C–O–C in glycosidic linkage in the range 896–1157 cm^{-1} [26].

FTIR spectra of SC scaffold show characteristic bands for wollastonite at 1022 and 1065 cm^{-1} corresponding to the asymmetric stretching mode of Si–O–Si, 645 cm^{-1} assigned to the symmetric stretching vibration of Si–O–Si and absorption bands located at 455 cm^{-1} and 564 cm^{-1} corresponding to the bending vibrational mode of Si–O–Si. Additional bands characteristic for wollastonite are observed at 984, 937 and 920 cm^{-1} corresponding to stretching non-bridging Si–O, and 710 cm^{-1} stretching bridging Si–O(Si) characteristic for the presence of 3-membered ring [27,28]. The FTIR spectra of composite scaffolds (SC_CHT and SC_CHT/sHAp) show characteristic bands for wollastonite, while the additional peaks and changes are the result of additional phases in the scaffolds, CHT and HAp. The presence of the HAp phase within chitosan matrix in the CHT/sHAp scaffold has been confirmed in our previous study [14]. However, in the range 800–1200 cm^{-1} it is hard to distinguish which band corresponds to a certain phase of wollastonite, HAp and CHT as all show characteristic bands in that

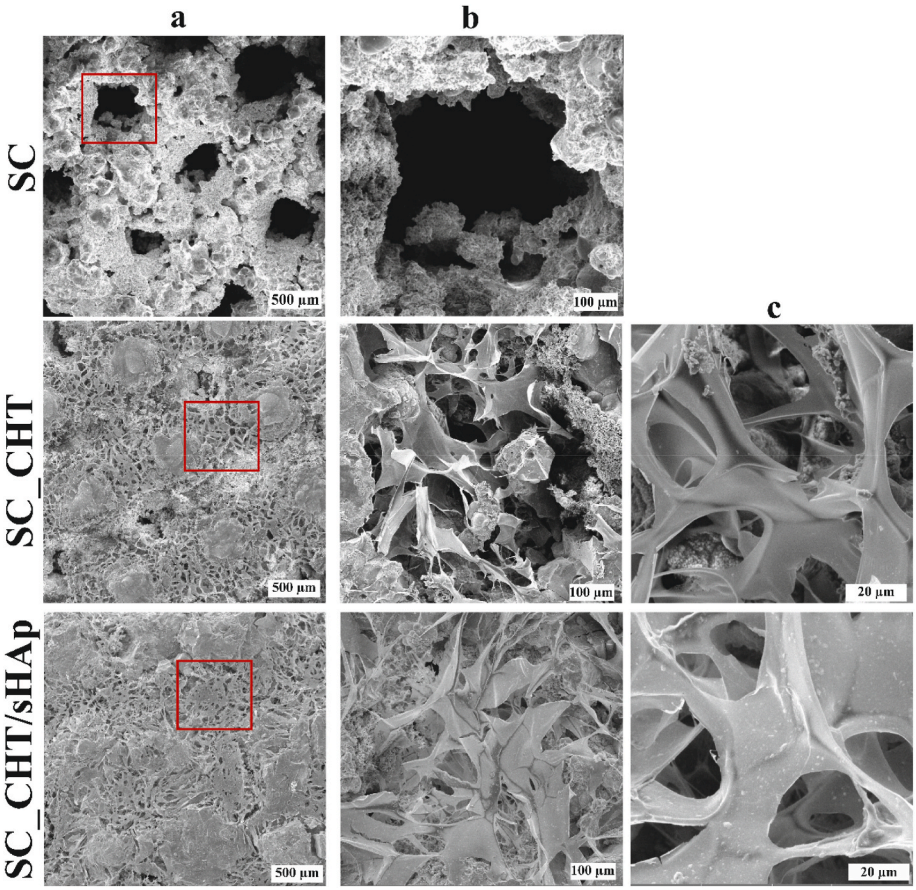

Fig. 3. Microscopic imaging of SC, SC_CHT and SC_CHT/sHAp scaffolds. The pores of 400 µm are depicted in red squares. Scale bar: 500 (a), 100 (b) and 20 µm (c). (For interpretation of the references to colour in this figure legend, the reader is referred to the Web version of this article.)

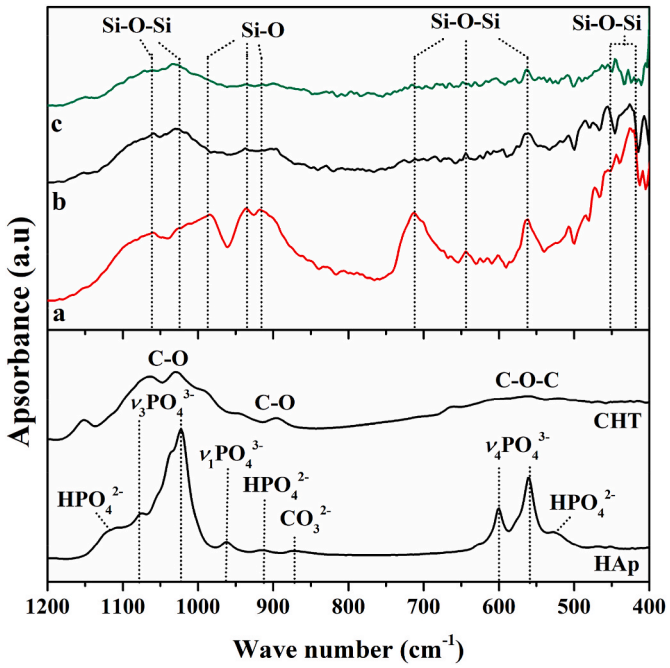

Fig. 4. FTIR spectra of prepared SC (a), SC_CHT (b) and SC_CHT/sHAp (c) scaffolds. Chitosan (CHT) and hydroxyapatite (HAp) were used as controls.

range. In addition, the low amount (as explained below) of HAp phase in the final SC_CHT/sHAp cannot be excluded as a reason for not detecting clear bands characteristic for PO_4^{3-} groups in HAp lattice.

3.4. EDX and element mapping of the prepared materials

EDX spectra (Fig. 5a) of HAp particles within the polymer matrix in SC_CHT/sHAp, confirmed the presence of calcium, phosphorus, oxygen, carbon and silicon in SC_CHT/sHAp. Additionally, the presence of sodium, selenium, magnesium, zinc and strontium ions has been detected as a result of preparing the mixture of four different mono-substituted HAps and biogenic source for HAp synthesis. The process of impregnation, neutralization and washing of the SC_CHT/sHAp scaffolds did not influence trace element content in HAp phase. As expected, EDX element mapping illustrates calcium (red) and phosphorus (yellow) detected in the HAp particles within the polymer matrix. Further, the carbon (illustrated in green) is observed in the polymer matrix and HAp particles, and could originate from chitosan or be a result of CO_3^{2-} substitution of HAp. The silicon, illustrated in blue, is observed within the chitosan matrix and it might be a result of silicon and wollastonite dissolution during material preparation. SC_CHT/sHAp scaffold preparation involves impregnation of the SC scaffold with CHT/sHAp solution (pH = 5.23) and neutralization in the NaOH/EtOH medium (pH > 10). The mineral dissolution and precipitation are influenced by H^+ (acid system) or OH^- (base system) environment [29]. Wollastonite ($CaSiO_3$) dissolution in acetic acid was described in the study by Ptáček et al. [30] according to Eq. (1):

$$CaSiO_3 + 2CH_3COOH \rightarrow Ca^{2+} + 2CH_3COO^- + SiO_2 + H_2O \quad (1)$$

However, the SEM analysis did not reveal additional SiO_2 particles

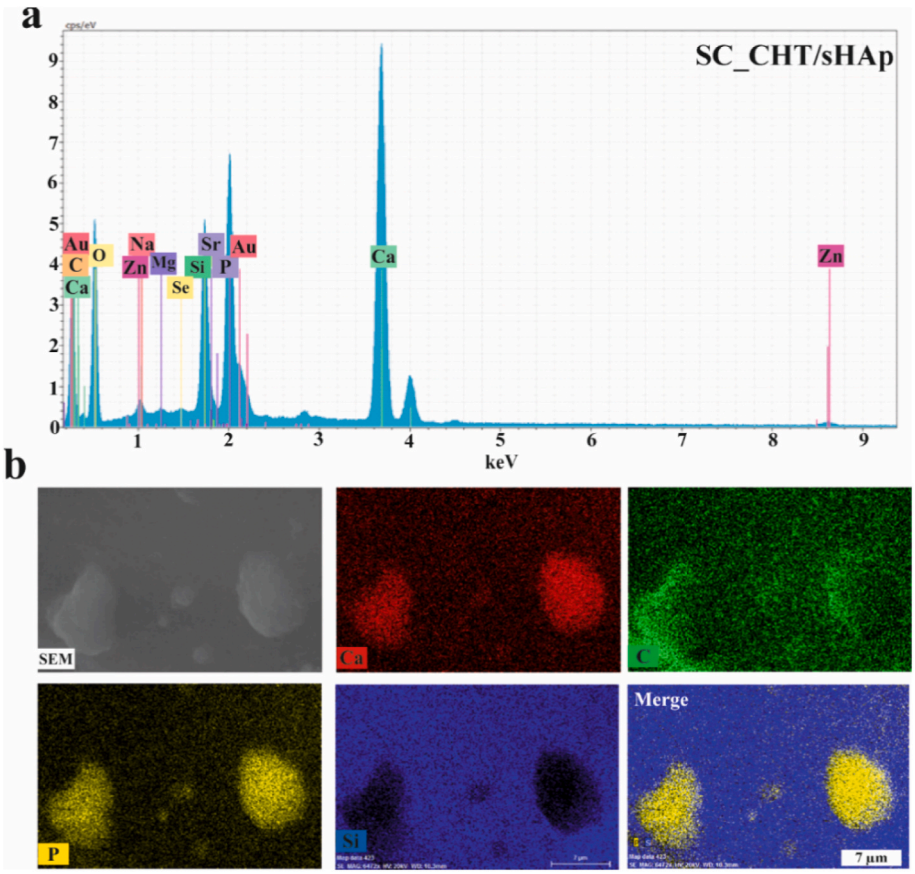

Fig. 5. EDX spectra (a) and elemental mapping (b) of calcium, phosphorus, carbon and silicon for HAp particles in composite scaffold SC_CHT/sHAp. (For interpretation of the references to colour in this figure legend, the reader is referred to the Web version of this article.)

on the chitosan surface as a result of $CaSiO_3$ dissolution. In addition, EDX elemental mapping detected silicon in the polymer matrix, while at the parts where HAp was detected, the silicon was not found. This indicates that the presence of silicon in the polymer matrix might not be the result of SiO_2 precipitation. However, the precipitation of nanometer SiO_2 particles, that cannot be detected by SEM and XRD analysis, cannot

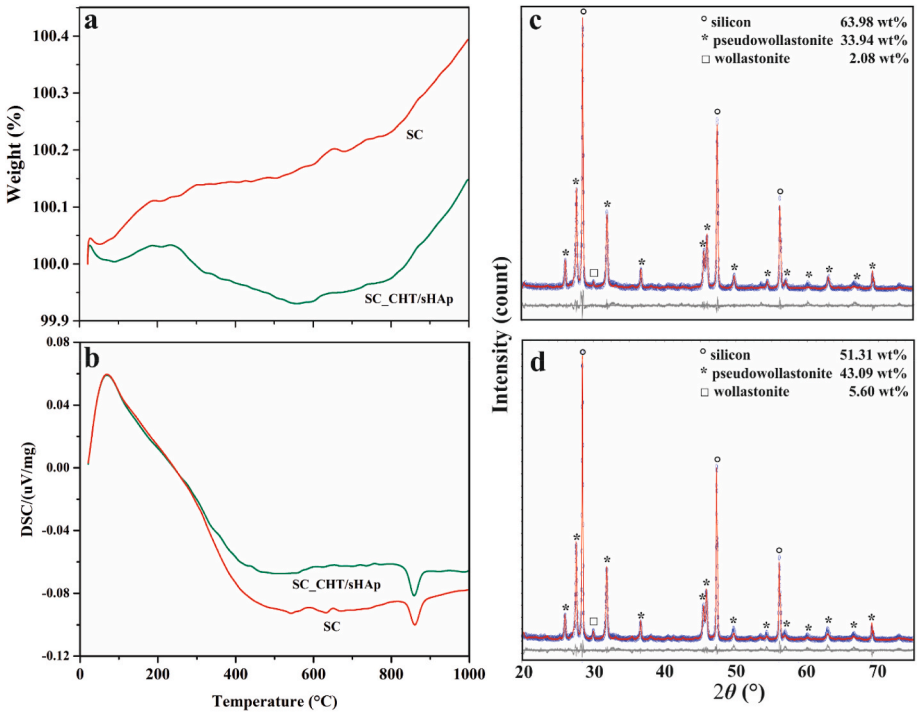

Fig. 6. Thermogravimetric (a) and differential scanning calorimetry (b) analysis of the SC and SC_CHT/sHAp scaffolds. Whole-powder pattern decomposition analysis of SC_CHT/sHAp scaffolds before (c) and after (d) thermogravimetric analysis. The solid lines (red) are calculated data intensities, and open circles (blue) are experimental dana intensities. Below the XRD profile, the difference between calculated and experimental intensities is plotted in gray. (For interpretation of the references to colour in this figure legend, the reader is referred to the Web version of this article.)

be fully excluded. In this case, the chitosan acts as a template for nano-SiO_2 precipitation. Turaferri et al. [31] studied the mechanism of chitosan adsorption on silica from aqueous solution at different pH values. As explained, in mild acidic solutions, chitosan behaves as a weakly charged polyelectrolyte, whereby electrostatic attraction is the main driving force for adsorption. Another possible explanation for detected silicon in the polymer matrix is partial solubility of Si in the NaOH (neutralization medium) and, consequently, the absorption of dissolved silicon ions by the chitosan matrix [32]. Chitosan is known to have a good complexing ability through the specific interactions of amino ($–NH_2$) and hydroxyl (–OH) groups that enable them to form strong interactions with heavy metals *via* coordination bonds [33]. However, due to the lack of studies on the adsorption process between chitosan and Si, future studies should be focused on understanding the mechanism of interactions. The presence of Si–OH layer on the surface of the biomaterials can enhance cell adhesion, as these groups could promote the functional representation of the integrin-binding domain of adsorbed proteins [34]. It seems from Fig. 5b that calcium and phosphorus are present not only within the HAp particles, but also in small concentrations in the matrix. It can be assumed that a part of the sHAp particles dissolved during homogenization with chitosan solution, due to acidic conditions [35], and that during the neutralization process in the gelation medium *in situ* precipitation of calcium phosphates occurred.

3.5. XRD and thermal analysis of composite scaffolds

TGA (Fig. 6a) and DSC (Fig. 6b) analyses were performed to determine the amount of CHT in the prepared composite scaffolds. The difference in TGA curves between SC and SC_CHT/sHAp scaffolds can be assigned to the decomposition of CHT occurring in the range of 180–400 °C. An increase in the weight after heating above 600 °C, especially after ~850 °C, indicates that changes in the phases occurred. After the composite scaffold preparation process, the crystalline phases detected in the SC_CHT/sHAp scaffold were silicon (63.98 wt%, ICSD 00-027-1402), pseudowollastonite (33.94 wt%, ICSD 04-012-1776), and wollastonite (2.08 wt%, ICSD 04-016-5334), the phases characteristic for SC scaffold (Fig. 6c). No additional crystalline phases were formed during SC_CHT/sHAp composite scaffold preparation. HAp phase was not detected by the XRD due to its low amount in the final SC_CHT/sHAp composite scaffold. Based on TGA analysis the amount of HAp phase of 0.06 wt% was estimated. After TGA/DSC analysis, the same crystalline phases were detected, however weight percentage of silicon decreased to 51.31 wt%, while the weight percentage for pseudowollastonite and wollastonite increased to 43.09 and 5.60 wt%, respectively (Fig. 6d). The SLM process of scaffold fabrication was performed under the high purity argon in order to avoid oxidation. TGA/DSC analyses were performed in the air flow resulting in the oxidation and increase of pseudowollastonite and wollastonite phase content.

3.6. Compression test

In Fig. 7a, the stress-strain curves of the obtained scaffolds are demonstrated. The stress-strain curves for composite materials (SC_CHT and SC_CHT/sHAp) begin with a linear elastic response followed by nonlinear behaviour with the applied stress as previously described [15]. The curves have a positive slope up to the highest stress, followed by a plunging trend pointing at the cracks development within scaffolds. The changes in the compressive strength of obtained scaffolds are shown in Fig. 7b. It can be observed that the compressive strength of composite scaffolds significantly decreased compared to the scaffold SC. The compressive strength decreased from 36.70 MPa for SC, to 30.75 and 30.25 MPa for SC_CHT and SC/CHT/sHAp, respectively. As previously mentioned, composite scaffold preparation involves steps where scaffolds are immersed in acid and basic solutions. The dissolution of silicon results in a decrease of compressive strength of SC_CHT and SC/CHT/sHAp scaffolds. The compressive strength of the composite scaffolds is greater than the strength of a trabecular bone (2–12 MPa) but less than the stress of cortical bone (100–230 MPa) [36–38]. The mechanical strength is a critical feature in bone regeneration and it is primarily controlled by pore volume and characteristics of used materials [13]. The current challenge in scaffold design for regeneration of large bone defects under load is to create a structure with large and interconnected pores while providing a compressive strength comparable to cortical bone [39]. Reported compressive modulus and strength of chitosan scaffolds differ vastly, and fall in the ranges of 0.0038–2.56 MPa and 0.059–0.125 MPa, respectively [40]. In our previous study [41], mechanical analyses of CHT/HAp scaffolds, with different weight ratios, have been performed. No substantial change in mechanical properties was achieved with HAp addition. For the CHT/HAp (70/30) scaffold compressive modulus of 4.8 ± 0.7 kPa was estimated that is significantly lower than the compressive modulus of bone, indicating that scaffolds can be used in small-size bone defects in no load-bearing applications. However, the SC_CHT/sHAp composite scaffold has higher mechanical properties and therefore can be used for a wider range of critical size bone defects.

3.7. Cytocompatibility assesment of the scaffolds

The *live/dead* assay was determined after 1 and 7 days of HEK 293 cell culture and is shown in Fig. 8. HEK 293 cells are commonly used cell lines in biomedical research since they are easy to grow and maintain offering very high reproducibility. After 1 day of the cell culture, the HEK 293 attachment on SC_CHT and SC_CHT/sHAp scaffolds was enhanced compared to the SC scaffold. After 7 days of cell culture, HEK

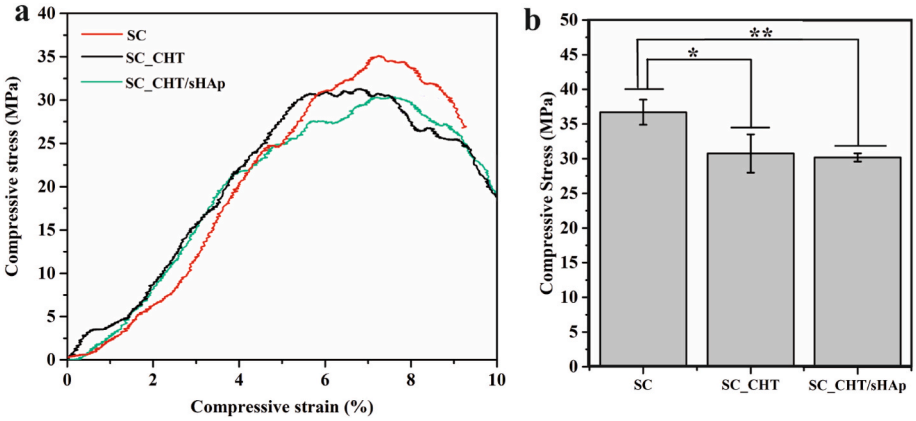

Fig. 7. Experimental stress-strain response (a) and changes in a compressive strength (b) of prepared scaffolds (n = 3). Significant difference between two groups: * ($p < 0.05$) and ** ($p < 0.01$).

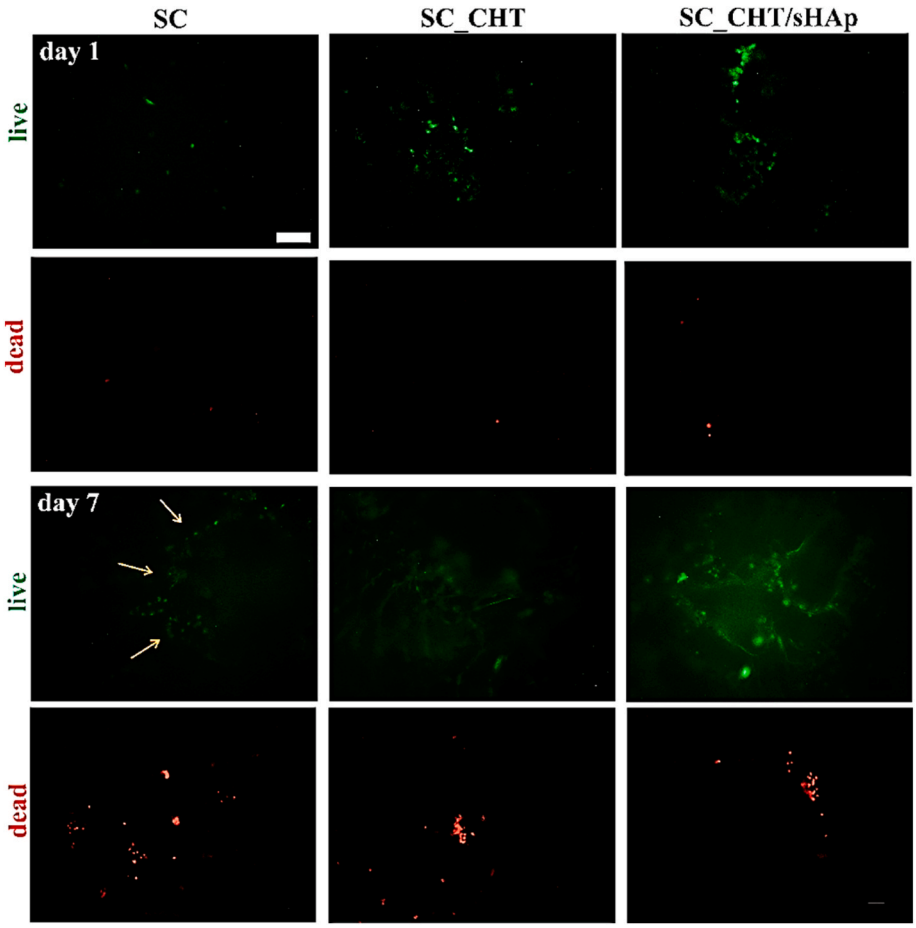

Fig. 8. *Live/dead* staining of seeded cells. The cell viability and distribution on obtained scaffolds after 1 and 7 days of culture. HEK 293 cells proliferation around the pore of the SC scaffold is depicted in orange arrows. Live cells are stained in green, dead cells are stained in red. Scale bar: 100 μm. (For interpretation of the references to colour in this figure legend, the reader is referred to the Web version of this article.)

293 cells (orange arrows) proliferated around the pore wall of the SC scaffold, while on the SC_CHT and SC_CHT/sHAp scaffolds cell proliferation was enhanced. Due to the presence of CHT/sHAp hydrogel within the pores, cell attachment and proliferation within pores are allowed, as hydrogel enables cell migration. Obtained micro- and macroporosity of CHT/sHAp hydrogel within SC scaffold pores enable cell seeding and migration, cell-cell and cell-matrix interaction. However, the migration of the cells through the scaffold volume needs to be confirmed by additional biological analysis. Further, as naturally derived polymers are components or have a similar structure as the organic part of natural bone tissue, they demonstrate appropriate biocompatibility and present a range of ligands and peptides that facilitate bone cell adhesion and osteospecific function [3]. After 1 day of cell culture, only a few dead cells were detected, while after 7 days of cell culture agglomerated dead cells were detected as a result of cell overgrowth at this part of the scaffolds. However, cell death due to overgrowth is not connected to material toxicity. The *live/dead* assay points out the advantages of combining SC scaffold with CHT/sHAp hydrogel to increase cell attachment and homogeneous proliferation. However, the osteogenic potential of the obtained composite scaffolds needs to be confirmed by using stem cells under dynamic conditions by using a perfusion bioreactor.

4. Conclusions

In our previous study, a biomimetic CHT/sHAp scaffold was developed in order to achieve molecular, structural and biological compatibility similar to that of natural bone tissue to facilitate bone regeneration. However, the produced highly porous CHT/sHAp hydrogel substituted with key role elements (Sr^{2+}, Mg^{2+}, Zn^{2+}, SeO_3^{2-}) were suitable for non-load bearing applications (e.g. maxillofacial defects). To increase both the mechanical properties of CHT/sHAp hydrogel and the biocompatibility of the SC scaffold, the composite SC_CHT/sHAp scaffold was obtained by impregnation and freeze gelation method. The composite scaffolds can be used for load-bearing applications due to the adequate compressive strength of ~30.25 MPa. Results indicate that the presence of chitosan in prepared scaffolds has a beneficial effect on cell attachment and proliferation. By ensuring both microporosity and macroporosity, obtained scaffolds ensure the environment for efficient cell seeding, migration and proliferation, vascularization and diffusion of nutrients and metabolic waste. The presented SC_CHT/sHAp scaffolds exhibit promising properties for the development of artificial bone graft substitutes.

Declaration of competing interest

The authors declare that they have no known competing financial interests or personal relationships that could have appeared to influence the work reported in this paper.

Acknowledgements

The authors are grateful to the JECS Trust for funding the visit of Antonia Ressler to Tallinn University of Technology (Contract No. 2020259). European Regional Development Fund Project bIDEAS (KK.01.1.1.07.0014) and Estonian Research Council (grant PRG643) are

gratefully acknowledged.

References

[1] T. Cordonnier, J. Sohier, P. Rosset, P. Layrolle, Biomimetic materials for bone tissue engineering – state of the art and future trends, Adv. Eng. Mater. 13 (2011) B135–B150, https://doi.org/10.1002/adem.201080098.

[2] I. Ratha, P. Datta, V.K. Balla, S.K. Nandi, B. Kundu, Effect of doping in hydroxyapatite as coating material on biomedical implants by plasma spraying method: a review, Ceram. Int. 47 (2021) 4426–4445, https://doi.org/10.1016/j.ceramint.2020.10.112.

[3] M.A. Fernandez-Yague, S.A. Abbah, L. McNamara, D.I. Zeugolis, A. Pandit, M. J. Biggs, Biomimetic approaches in bone tissue engineering: integrating biological and physicomechanical strategies, Adv. Drug Deliv. Rev. 84 (2015) 1–29, https://doi.org/10.1016/j.addr.2014.09.005.

[4] A. Ressler, A. Žužić, I. Ivanišević, N. Kamboj, H. Ivanković, Ionic substituted hydroxyapatite for bone regeneration applications: a review, Open Ceramics 6 (2021), 100122, https://doi.org/10.1016/j.oceram.2021.100122.

[5] B. Wopenka, J.D. Pasteris, A mineralogical perspective on the apatite in bone, Mater. Sci. Eng. C 25 (2005) 131–143, https://doi.org/10.1016/j.msec.2005.01.008.

[6] S. Bose, G. Fielding, S. Tarafder, A. Bandyopadhyay, Understanding of dopant-induced osteogenesis and angiogenesis in calcium phosphate ceramics, Trends Biotechnol. 10 (2013) 594–605, https://doi.org/10.1016/j.tibtech.2013.06.005.

[7] C.K.S. Pillai, W. Paul, S.P. Sharma, Chitin and chitosan polymers: chemistry, solubility and fiber formation, Prog. Polym. Sci. 34 (2009) 641–678, https://doi.org/10.1016/j.progpolymsci.2009.04.001.

[8] H. Tan, C.R. Chu, K.A. Payne, K.G. Marra, Injectable in situ forming biodegradable chitosan-hyaluronic acid based hydrogels for cartilage tissue engineering, Biomaterials 30 (2009) 2499–2506, https://doi.org/10.1016/j.biomaterials.2008.12.080.

[9] R. Mansouri, Y. Jouan, E. Hay, C. Blin-Wakkach, A. Ostertag, C. Le Henaff, C. Marty, V. Geoffroy, P.J. Marie, M. Co-hen-Solal, D. Modrowski, Osteoblastic heparan sulfate glycosaminoglycans control bone remodeling by regulating Wnt signaling and the crosstalk between bone surface and marrow cells, Cell Death Dis. 8 (2017), e2902, https://doi.org/10.1038/cddis.2017.287.

[10] S. Islam, M.A.R. Bhuiyan, M. N Islam, Chitin and chitosan: structure, properties and applications in biomedical engineering, J. Polym. Environ. 25 (2017) 854–866, https://doi.org/10.1007/s10924-016-0865-5.

[11] L. Pighinelli, M. Kucharska, Chitosan–hydroxyapatite composites, Carbohydr. Polym. 93 (2013) 256–262, https://doi.org/10.1016/j.carbpol.2012.06.004.

[12] S.L. Levengood, M. Zhang, Chitosan-based scaffolds for bone tissue engineering, J. Mater. Chem. B 2 (2014) 3161–3184, https://doi.org/10.1039/C4TB00027G.

[13] L. Roseti, V. Parisi, M. Petretta, C. Cavallo, G. Desando, I. Bartolotti, B. Grigolo, Scaffolds for bone tissue engineering: state of the art and new perspectives, Mater. Sci. Eng. C 78 (2017) 1246–1262, https://doi.org/10.1016/j.msec.2017.05.017.

[14] A. Ressler, M. Antunović, L. Teruel-Biosca, G. Gallego Ferrer, S. Babić, I. Urlić, M. Ivanković, H. Ivanković, Osteogenic differentiation of human mesenchymal stem cells on substituted calcium phosphate/chitosan composite scaffolds, Carbohydr. Polym. 277 (2022), 118883, https://doi.org/10.1016/j.carbpol.2021.118883.

[15] N. Kamboj, J. Kazantseva, R. Rahmani, M.A. Rodríguez, I. Hussainova, Selective laser sintered bio-inspired silicon-wollastonite scaffolds for bone tissue engineering, Mater. Sci. Eng. C 116 (2020), 111223, https://doi.org/10.1016/j.msec.2020.111223.

[16] S.V. Dorozhkin, Calcium orthophosphates ($CaPO_4$): occurrence and properties, Prog. Biomater. 5 (2016) 9–70, https://doi.org/10.1007/s40204-015-0045-z.

[17] A. Rogina, L. Pribolšan, A. Hanžek, L. Gomez-Estrada, G. Gallego Ferrer, I. Marijanović, M. Ivanković, H. Ivanković, Macroporous poly(lactic acid) construct supporting the osteoinductive porous chitosan-based hydrogel for bone tissue engineering, Polymer 98 (2016) 172–181, https://doi.org/10.1016/j.polymer.2016.06.030.

[18] A. Ressler, A. Gudelj, K. Zadro, M. Antunović, M. Cvetnić, M. Ivanković, H. Ivanković, From bio-waste to bone substitute: synthesis of biomimetic hydroxyapatite and its use in chitosan-based composite scaffold preparation, Chem. Biochem. Eng. Q. 34 (2020) 59–71, https://doi.org/10.15255/CABEQ.2020.1783.

[19] L.J. Vaselinović, L.J. Kranović, Z. Stojanović, I. Bračko, S. Marković, N. Ignjatović, D. Uskoković, Crystal structure of cobalt-substituted calcium hydroxyapatite nanopowders prepared by hydrothermal processing, J. Appl. Crystallogr. 43 (2010) 320–327.

[20] A. Farzadi, F. Bakhshi, M. Solati-Hashjin, M. Asadi-Eydivand, N.A. abu Osman, Magnesium incorporated hydroxyapatite: synthesis and structural properties characterization, Ceram. Int. 40 (2014) 6021–6029, https://doi.org/10.1016/j.ceramint.2013.11.051.

[21] I. Cacciotti, A. Bianco, M. Lombardi, L. Montanaro Mg-substituted hydroxyapatite nanopowders: synthesis, thermal stability and sintering behaviour, J. Eur. Ceram. 29 (2009) 2969–2978, https://doi.org/10.1016/j.jeurceramsoc.2009.04.038.

[22] V. Uskoković, M.A. Iyer, V.M. Wu, One ion to rule them all: the combined antibacterial, osteoinductive and anticancer properties of selenite-incorporated hydroxyapatite, J. Mater. Chem. B 5 (2017) 1430–1445, https://doi.org/10.1039/C6TB03387C.

[23] M.P. Moreira, G.D. de Almeida Soares, J. Dentzer, K. Anselme, L.A. de Sena, A. Kuznetsov, E.A. dos Santos, Synthesis of magnesium- and manganese-doped hydroxyapatite structures assisted by the simultaneous incorporation of strontium, Mater. Sci. Eng. C 62 (2016) 736–743, https://doi.org/10.1016/j.msec.2016.01.004.

[24] A. Rogina, P. Rico, G. Gallego Ferrer, M. Ivanković, H. Ivanković, Effect of in situ formed hydroxyapatite on microstructure of freeze-gelled chitosan-based biocomposite scaffolds, Eur. Polym. J. 68 (2015) 278–287, https://doi.org/10.1016/j.eurpolymj.2015.05.004.

[25] E. Landi, G. Celotti, G. Logroscino, A. Tampieri, Carbonated hydroxyapatite as bone substitute, J. Eur. Ceram. Soc. 23 (2003) 2931–2937, https://doi.org/10.1016/S0955-2219(03)00304-2.

[26] H.F.G. Barbosa, D.S. Francisco, A.P.G. Ferreira, E.T.G. Cavalheiro, A new look towards the thermal decomposition of chitins and chitosans with different degrees of deacetylation by coupled TG-FTIR, Carbohydr. Polym. 225 (2019), 115232, https://doi.org/10.1016/j.carbpol.2019.115232.

[27] W. Chen, Y. Liang, X. Hou, J. Zhang, H. Ding, S. Sun, H. Cao, Mechanical grinding preparation and characterization of TiO2-coated wollastonite composite pigments, Materials 11 (2018) 593, https://doi.org/10.3390/ma11040593.

[28] A. Bianco, I. Cacciotti, M. Lombardi, L. Montanaro, Si-substituted hydroxyapatite nanopowders: synthesis, thermal stability and sinterability, Mater. Res. Bull. 44 (2009) 345–354, https://doi.org/10.1016/j.materresbull.2008.05.013.

[29] M.Z. Kashim, H. Tsegab, O. Rahmani, Z.A. Abu Bakar, S.M. Aminpour, Reaction mechanism of wollastonite in situ mineral carbonation for CO2 sequestration: effects of saline conditions, temperature, and pressure, ACS Omega 5 (45) (2020) 28942–28954, https://doi.org/10.1021/acsomega.0c02358.

[30] P. Ptáček, M. Nosková, J. Brandštetr, F. Šoukal, T. Opravil, Dissolving behavior and calcium release from fibrous wollastonite in acetic acid solution, Thermochim. Acta 498 (2010) 54–60, https://doi.org/10.1016/j.tca.2009.10.002.

[31] A. Tiraferri, P. Maroni, D. Caro Rodriguez, M. Borkovec, Mechanism of chitosan adsorption on silica from aqueous solutions, Langmuir 30 (2014) 4980–4988, https://doi.org/10.1021/la500680g.

[32] C. Lai, Z. Xiang, C. Liu, C. Zhu, H. Wang, H. Zhu, Study on corrosion of macroporous silicon in sodium hydroxide solution by electrochemical methods and scanning electron microscopy, Int. J. Corros. 2015 (2015), 375489, https://doi.org/10.1155/2015/375489.

[33] R.C. Fai Cheung, T. Bun Ng, J. Ho Wong, W. Yee Chan, Chitosan: an update on potential biomedical and pharmaceutical applications, Mar. Drugs 13 (2015) 5156–5186, https://doi.org/10.3390/md13085156.

[34] B.S. Kim, S.S. Yang, J.H. Yoon, J. Lee, Enhanced bone regeneration by silicon-substituted hydroxyapatite derived from cuttlefish bone, Clin. Oral Implants Res. 28 (2017) 49–56, https://doi.org/10.1111/clr.12613.

[35] S.V. Dorozhkin, Dissolution mechanism of calcium apatites in acids: a review of literature, World J. Methodol. 2 (2012) 1–17, https://doi.org/10.5662/wjm.v2.i1.1.

[36] G. Turnbull, J. Clarke, F. Picard, P. Riches, L. Jia, F. Han, B. Li, W. Shu, 3D bioactive composite scaffolds for bone tissue engineering, Bioact. Mater. 3 (2018) 278–314, https://doi.org/10.1016/j.bioactmat.2017.10.001.

[37] J. Jacob, N. More, K. Kalia, G. Kapusetti, Piezoelectric smart biomaterials for bone and cartilage tissue engineering, Inflamm. Regen. 38 (2018) 2, https://doi.org/10.1186/s41232-018-0059-8.

[38] J. Henkel, M.A. Woodruff, D.R. Epari, R. Steck, V. Glatt, I.C. Dickinson, P.F. M. Choong, M.A. Schuetz, D.W. Hutmacher, Bone regeneration based on tissue engineering conceptions — a 21st century perspective, Bone Res 1 (2014) 216–248, https://doi.org/10.4248/br201303002.

[39] S.I. Roohani-Esfahani, P. Newman, H. Zreiqat, Design and fabrication of 3D printed scaffolds with a mechanical strength comparable to cortical bone to repair large bone defects, Sci. Rep. 6 (2016), 19468, https://doi.org/10.1038/srep19468.

[40] S. Jana, S.J. Florczyk, M. Keung, M. Zhang, High-strength pristine porous chitosan scaffolds for tissue engineering, J. Mater. Chem. 22 (2012) 6291, https://doi.org/10.1039/C2JM16676C.

[41] A. Rogina, P. Rico, G. Gallego Ferrer, M. Ivanković, H. Ivanković, In situ hydroxyapatite content affects the cell differentiation on porous chitosan/hydroxyapatite scaffolds, Ann. Biomed. Eng. 44 (2016) 1107–1119, https://doi.org/10.1007/s10439-015-1418-0.